

Multitemporal Sentinel-1 and Sentinel-2 Images for Characterization and Discrimination of Young Forest Stands Under Regeneration in Norway

Vahid Akbari , Member, IEEE, Svein Solberg, and Stefano Puliti

Abstract—There is a need for mapping of forest areas with young stands under regeneration in Norway, as a basis for conducting tending, or precommercial thinning (PCT), whenever necessary. The main objective of this article is to show the potential of multitemporal S-1 and S-2 data for characterization and detection of forest stands under regeneration. We identify the most powerful radar and optical features for discrimination of forest stands under regeneration versus other forest stands. A number of optical and radar features derived from multitemporal S-1 and S-2 data were used for the class separability and cross-correlation analysis. The analysis was performed on forest resource maps consisting of the forest development classes and age in two study sites from south-eastern Norway. Important features were used to train the classical random forest (RF) classification algorithm. A comparative study of performance of the algorithm was used in three cases: I) using only S-1 features, II) using only S-2 optical bands, and III) using combination of S-1 and S-2 features. RF classification results pointed to increased class discrimination when using S-1 and S-2 data in relation to S-1 or S-2 data only. The study shows that forest stands under regeneration in the height interval for PCT can be detected with a detection rate of 91% and F-1 score of 73.2% in case III as most accurate, while tree density and broadleaf fraction could be estimated with coefficient of determination (R^2) of about 0.70 and 0.80, respectively.

Index Terms—Forest stands under regeneration, precommercial thinning (PCT), radar backscattering coefficient, random forest (RF) classification, remote sensing, repeat-pass interferometric coherence magnitude, Sentinel-1 (S-1), Sentinel-2 (S-2), spectral bands, synthetic aperture radar (SAR).

I. INTRODUCTION

THERE is a need for mapping of forest areas with young stands under regeneration, in order to ensure that required precommercial thinning (PCT) is carried out. The objective of PCT is to enhance the growth of the most commercially valuable trees by reducing the density of undesired trees that compete for light, water, and nutrients [1]. Such forest management decisions are made for forest stands, which represent the minimum area unit for forest management and are generally small and

homogeneous forest areas [0.5–10 hectares (ha)]. In many cases, there is a need to remove a number of small trees to get an appropriate stand density, correct tree species or mixture, and evenly distributed trees over the area, as well as to remove trees having unwanted properties such as damage, diseases, and poor quality [2]–[4]. Typically, young stands of Norway spruce have a considerable inmixing of broadleaved trees, whose growth rate at low age competes with the spruce trees. In other cases, there are too many trees of Norway spruce or Scots pine due to natural regeneration without plantation. Based on forest management statistics forest authorities have for many years reported blue to low tending activity. Without doing anything, the long-term consequences can be a low forest production, poor timber quality, and high risk for snow and wind damage [5], [6]. We have seen a decrease in the number of foresters and the time they spend in the forest, and this increases the need for digital forest data.

By selecting the future crop trees, PCT operations are key to ensure the future value of a forest stand. Knowledge on where to perform PCT is, thus, important in a context of precision forestry [1]. Currently in Norway, field visits are carried out by local forest managers to determine whether to perform PCTs or not. However, such methods are subjective and costly; thus, new methods based on the use of remotely sensed data have been proposed. Drones are being increasingly used for information management in regeneration forests [7]. However, their use can be applied only at a local scale on selected forest stands. On the other end of the scale, there is the need for regional or even national maps to provide insights in which are the potential areas requiring PCTs. Within this context, satellite remote sensing can provide an important tool for effective and low-cost monitoring of young forest stands. The availability, frequency, and coverage of satellite remote sensing data have increased considerably during the last years, in particular due to the European Union's Copernicus program with the Sentinel-1 (S-1) and Sentinel-2 (S-2) [8], [9]. Optical images, like from S-2, typically have the advantage of being largely designed for forest and vegetation monitoring [7], [10]–[12] because of their high spatio-temporal resolution, wide spatial coverage, and broad spectrum. However, they are severely affected by cloud cover and meteorological conditions, and they are dependent on solar illumination, so it is difficult to acquire adequate and clear S-2 images in boreal and high latitude areas. The optical data can be supplemented with data from synthetic aperture radar

Manuscript received July 11, 2020; revised September 20, 2020, January 27, 2021, and February 27, 2021; accepted April 11, 2021. Date of publication April 15, 2021; date of current version May 26, 2021. This work was supported in part by Norskog under Grant 11281 and in part by the “Copernicus Program in Norway” under Grant 51567. (Corresponding author: Vahid Akbari.)

The authors are with the Norwegian Institute of Bioeconomy Research, 1431 Ås, Norway (e-mail: va2akbari@gmail.com; svein.solberg@nibio.no; stefano.puliti@nibio.no).

Digital Object Identifier 10.1109/JSTARS.2021.3073101

(SAR) sensors, like S-1, which in general are unaffected by day–night, clouds, and almost any weather condition. Despite a completely different measurement method, SAR is promising for mapping and monitoring of forests [13], [14], in particular for stem volume and biomass estimation [15]–[17]. However, terrain topography has a significant impact on the geometric and radiometric qualities of SAR images [18], [19].

A S-1 satellite with a C-band and dual-polarization (VV/VH) sensor provides a promising opportunity for mapping of forest stands at no cost. Some studies reported that the backscatter coefficients and interferometric SAR (InSAR) coherence magnitude in SAR time series are the most useful SAR features in land cover classification [20]–[22]. An important implication here is that these parameters are influenced by forest structure and age [23]. Several authors have investigated the possibility to model forest age using SAR backscattering intensity [16],[24], [25]. Radar backscattering coefficient is expected to increase with increasing tree height and age and, therefore, can be used to map forest age [25]–[27]. Pulliainen *et al.* [28] showed that the mean backscattering intensity of several ERS-1 images increases with forest volume. In another study, Quegan *et al.* [24] assessed the potential of time series of the C-band SAR backscattering coefficient for forest biomass mapping. Furthermore, they noted a relationship between forest stand age and backscatter: the scattering from the soil decreases with the growing age, resulting in a reduction of the overall backscatter. Authors in [26] and [27] used the SAR backscatter data combined with Landsat TM data for mapping regenerating forest stages and concluded that the combination of SAR and optical bands was essential for the discrimination between regenerating forest stages.

The potential of C-band multitemporal interferometric coherence observations for land-cover mapping became evident after the launch of ERS-1 in 1991. A large number of studies confirmed the high potential of repeat-pass coherence magnitude calculated from multitemporal InSAR data for biomass estimation, forest-type classification, and clear-cut (CC) detection [29]–[31]. Authors in [24],[30], and [32]–[34] showed that C-band repeat-pass coherence acquired at short-term intervals shows a decline with increasing biomass. For different forest stands, the coherence decreases with an increase in the number of leaves, needles, and small branches in the stand. It was shown in [35] that multitemporal InSAR data are very well suited to stem volume retrieval in boreal forests. Santoro *et al.* [36] underlined the exponential relationship between ERS 1/2 tandem coherences and the stem volume. In another study, Pinto *et al.* [23] investigated the use of repeat-pass interferometric coherence to model forest age using NASA's L-band uninhabited aerial vehicle synthetic aperture radar (UAVSAR) datasets. Their results indicated that coherence measurements from L-band repeat-pass systems can estimate forest age accurately and with no saturation.

Given these observations and the fact that forest structure changes with age, it is conceivable that interferometric coherence magnitude and the backscattering coefficient could be used to map the forest age. The joint use of repeat-pass coherence and the backscattering coefficient allows better discrimination of forest stands that cannot be deduced by considering intensity

or coherence alone. Therefore, the S-1 backscatters and InSAR coherence magnitude from all within-year observations are employed to map forest age classes and to detect young stands under regeneration in need of PCT.

The spectral reflectance of forest canopies in optical remote sensing data has been measured and modeled to understand the relationship between spectral signatures and forest parameters, e.g., [37] and [38]. It has been shown that the forest reflectance generally decreases with the height and age of trees. During the early growth stage of forest stands, the satellite signal is mainly dominated by the reflectance coming from the ground vegetation, exposed soil, or rocks. As height increases and trees grow more, the canopies close, the ground vegetation becomes less dominant in the reflectance characteristics, and total leaf area of the canopy becomes dominant. Height growth comes into effect mostly through the amount of internal shadowing, especially in the shortwave infrared (SWIR) wavelengths because of good atmospheric penetration [5]. This study also aims to show the potential of the spectral characteristics of S-2 to discriminate young stands under regeneration from older stands and CCs.

Of the machine-learning algorithms, the random forest (RF) [39], [40] is an exceptionally flexible ensemble learning method that has been gaining attention in forest-type classifications [41]. RF can effectively handle high-dimensional, noisy, and multisource datasets without overfitting and achieving higher classification accuracy than other well-known classifiers, such as support vector machines [42] and k-nearest neighbors [43], while the estimated importance of variables in the classification can be used to analyze the input features. Moreover, RF is a simple classifier for parameter settings and requires no sophisticated parameter tuning. The main objective of this study is to characterize and detect young regenerated forests (REF) from the other forest stands in need of PCT using multitemporal S-1 and S-2 data. Three cases have been tested for the RF classification: I) only Sentinel-1 features, II) only S-2 spectral bands, and III) combination of S-1 and S-2 features.

The remainder of this article is organized as follows. Section II describes the study areas, datasets, preprocessing workflow, and the algorithm used for supervised classification and regression. Results and discussions are presented in Section III. Section IV concludes this article.

II. MATERIAL AND METHODS

A. Study Sites

We selected two study areas from the south-eastern part of Norway. The first study site was located in Ås municipality in the Viken county. This area was located between latitudes 59°35.9'N–59°45.7'N and longitudes 10°40.8'E–10°55.2'E. The second study side was located in Romedal with a center coordinate of 60°37.5'N, 11°30.0'E, and is a part of Stange municipality in the Innlandet county.

The areas are characterized by terrain heights ranging from 250–600 m above the sea level. The climate is continental with cold and snowy winters and warm and somewhat dry summers. The geology is dominated by shallow till on bedrock with gneiss and granite. The forest is dominated by Norway spruce

(*Picea abies* (L.) Karst.) followed by scots pine (*pinus sylvestris* L.) mixed with a smaller fraction of various broadleaved tree species. The forest management is based on stands with a mean area of 2.5 ha, and these are typically fairly even-aged and homogeneous with regard to tree species composition and site productivity.

B. Reference Data

As ground reference, we had two datasets, i.e., forest resource maps used in the first step (detecting forest stands under regeneration in the relevant height stage), and a field inventory in some selected forest stands under regeneration for the second step (classifying the need for PCT/tending).

For both study areas, we obtained access to a forest resource map consisting of forest stand polygons and a number of key attributes for each stand such as forest age class, site index, total volume, pine, spruce, and deciduous volume, and registration date. The forest resource maps were generated from forest planning companies, and they used image matching with aerial photographs for stand delineation. The forest resource dataset for Ås was made based on aerial imagery in 2007 and airborne laser scanning in 2009. The forest resource dataset for Romedal was based on airborne imagery and laser scanning in 2017. An example of a forest resource map in Ås municipality is shown in Fig. 1(a). We projected these datasets as forest resource data to the year 2018, by using a state-of-the-art program for forest growth modeling, and CC data taken from Global Forest Watch (GFW) [44]. For each stand, the forest resource data contained the developmental stage and the state of forest stands of five maturity classes, which are defined in the National Forest Inventory (NFI)'s field work protocol as follows [45], [46]:

- class I: CC;
- class II: REF;
- class III: young production forest (YPF);
- class IV: older production forest (OPF); and
- class V: old forest (OF).

Forest growth varies with age, tree species, and site productivity, and the maturity class of a stand is set based on these three properties. Within the context of this study, we refer to stands in the development of class II, as stands that have been harvested and where the next tree generation is regenerated either through planting or through natural seed dispersal, and where the dominant trees have not yet reached the merchantable size [1]. Such forest stands account for 17% (or 15.1 mill. ha) of the total productive forest area in Norway [45]. We identified stands in the development stage for tending as stands having mean tree height between 1.3 and 6.0 m. This made up a fraction of age class II. For each site index class, we used forest growth models to select age intervals where the trees would be within these height limits. On intermediate and high site index, we expected the main driver for tending to be fast growing broadleaves represented by growth curves for birch [47], while for low site index classes we considered the height growth of spruce [48] to be the main driver.

We carried out a field inventory, where we measured: first, the number of trees per ha for spruce, pine, and broadleaved

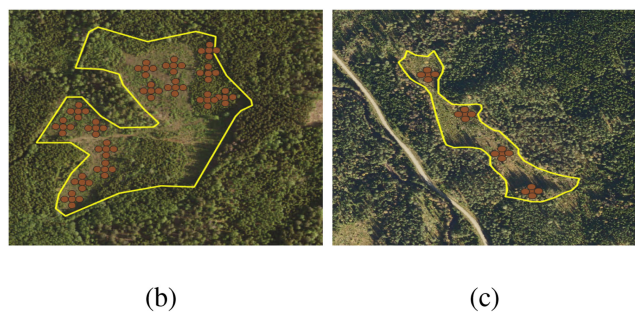
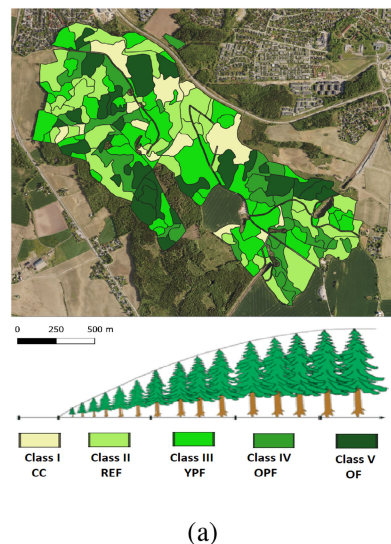


Fig. 1. (a) Example of a forest resource map in Ås municipality over an orthophoto image showing reference classes, where class I= CC; class II= REF; class III= YPF; class IV = OPF; and class V= Old Forest (OF). (b) and (c) Two example stands showing the field plot design. Yellow color: stand outline. Brown points: field plot clusters.

species, and, second, the tree density per ha for the same tree species [1]. The field plot measurements included trees having heights of at least 50 cm. We collected the field-plot dataset based on a systematic and clustered sampling design. Each cluster was composed of five 50 m² circular field plots, i.e., one located in the center of the cluster and the remaining four at a 10 m distance in each cardinal direction. Each field plot was subdivided into four quadrants of 12.5 m² each according to the cardinal directions. In total, the field-plot data comprised 217 clusters and 1084 plots. Two sample stands including field plots located in our test sites are shown in Fig. 1(b) and (c).

C. Sentinel-1 Data

The European Space Agency (ESA) has developed the Copernicus program which is currently composed of six Sentinel missions. S-1 Terrain Observation with Progressive Scan (TOPS) [49], [50] mode data shows its importance for forest mapping and monitoring. S-1 maintains a systematic routine operation that covers almost the entire land area on the Earth. The wide swath coverage of S-1 provides an efficient tool for monitoring forest stands at national and regional scales. For

TABLE I

SUMMARY OF S-1 A/B IW SLC DATA: RELATIVE ORBIT NUMBER (RON), ORBITAL PASS IN ASCENDING (ASC), OR DESCENDING (DSC) MODES, PERIOD OF OBSERVATION BETWEEN START AND END DATES AND THE NUMBER OF ACQUISITIONS (SLC) INVOLVED, SUBSWATHS (SW) USED AT EACH SITE

Site location	RON	Orbit pass	Start	End	No. SLC	SW
Romedal	139	DSC	20180103	20181229	60	IW1&IW2
Ås	139	DSC	20180103	20181229	60	IW2
Romedal	146	ASC	20180103	20181229	122	IW2
Ås	146	ASC	20180103	20181229	61	IW2

interferometric applications and time series analysis, it is desired to have a short temporal baseline and high coherence. Both S-1 A and S-1B provide 12 revisiting times, and the combined revisiting time between S-1 A and S-1B is 6 days. Together this generates 8 images for every 12-day period in the southern part of Norway by combining four relative orbits. S-1 SLC products consist of focused SAR data provided in slant-range geometry with an original spatial resolution of 3×22 m in range and azimuth, respectively.

All S-1 SLC IW images in both ascending and descending orbits and VV/VH polarization configuration covering both study areas from the year 2018 were downloaded from the Copernicus Open Access Hub¹ using Python API *Sentinelsat*.² This study uses 122 ascending and 60 descending images from the 139th and 146th relative orbits between January 3, 2018 and December 29, 2018. The period of time and the amount of preprocessed data considered per site are summarized in Table I.

D. Preprocessing of Sentinel-1 Data

The preprocessing steps carried out with the input SLC S-1 data were as follows.

1) *TOPS Splitting and Update of Orbits*: The entire processing workflow is generated using the Sentinel Application Platform (SNAP)³ Graph Builder interface. As the S-1 TOPSAR SLC image is formed by several bursts and three subswaths, we extracted the desired AOI with minimum number of bursts, and whenever possible within a single subswath in order to minimize the processing time. Initial processing steps involved the splitting of S-1 IW SLC data. Each TOPS scene was first split by defining subswath, polarization, and bursts covering the AOI. At the same time, we applied the orbit correction using the Apply Orbits operator.

2) *TOPS Geocoded Radar Backscatter*: The SAR image processing chain consists of the following six steps: 1) radiometric calibration to obtain σ^0 (σ^0); 2) thermal noise removal; 3) TOPSAR deburst; 4) subsetting; 5) range Doppler terrain correction against the geometric distortions (layover, foreshortening, and shadow); and 6) convert SAR backscatter intensities into decibel-scale (dB). Terrain correction was conducted using the recently released digital terrain model (DTM) of 10 m pixel spacing produced by the Norwegian mapping authority.⁴ The

image pixels were obtained at the final geocoded pixel spacing of 10×10 m in the Universal Transverse Mercator (UTM) coordinate system.

3) *TOPS Coregistration and Geocoded Coherence Magnitude*: The repeat-pass interferometric coherence magnitude describes the degree of correlation between two SAR acquisitions and, for this reason, it represents the key indicator to assess the quality of the interferometric phase. Under the assumption of ergodicity [51], the coherence magnitude of two SLC acquisitions, which are precisely coregistered at the subpixel level, is estimated for each pixel over a local neighborhood of complex scattering vectors $z(1), z(2), z(3), \dots, z(N)$ from a spatial neighborhood centered at pixel s :

$$\rho(z_1, z_2) = \left| \frac{\sum_{i \in W} z_1(i) z_2(i)^\dagger}{\sqrt{\sum_{i \in W} |z_1(i)|^2 \sum_{i \in W} |z_2(i)|^2}} \right|, \quad 0 \leq \rho \leq 1 \quad (1)$$

where z_1 is the complex value of a pixel in the first acquisition, and z_2 is the corresponding complex value in the second acquisition. $|\cdot|$ and \dagger denote the absolute value and the complex conjugate, respectively, and N represents the number of pixels in window W . We computed repeat-pass coherence magnitude for all images that were 6-day neighbors in time, and here we refer to the two images as master and slave. Each master–slave was used to create two independent stacks, one for the pair of master and coregistered slave SLCs and a second for the corresponding coherence generation [52]. The TOPS coregistration includes geometric coregistration of two S-1 SLC split products (master and slave) of the same subswath using the orbits of two products and a DTM. The coherence estimation was calculated using a box-car filter with three samples in azimuth and ten samples in range. Debursting of both the SLCs and the estimated coherence is carried out to obtain spatially continuous images. Spatial subsetting is applied to the coregistered and debursting coherence. Finally, terrain correction is again conducted to obtain precise geocoded coherence magnitude at pixel spacing of 10 m. If the AOI covers more than one subswath, the processing steps can be extended by processing and merging multiple swaths.

4) *Multitemporal Stack of Products*: When properly stacked data from a time series of radar data are available, it is recommended to preprocess time series data stacks with a multitemporal speckle filter [53]. It was already demonstrated in [54] that using the time series for a full year significantly increases the classification accuracy of forest versus nonforest compared to a single scene. The authors also concluded that the classification accuracy can further be improved when only considering the annual mean of multitemporal copolarized (VV) and cross-polarized (VH) backscatters. With M number of SLC SAR

¹[Online]. Available: <https://scihub.copernicus.eu/dhus/>

²[Online]. Available: <https://sentinelsat.readthedocs.io/en/stable/>

³SNAP software: [Online]. Available: <http://step.esa.int/main/download/>

⁴[Online]. Available: <https://hoydedata.no/LaserInnsyn/>

images, the correlation coefficient ρ in (1) can be computed temporally. The use of temporal averaging allowed us to provide more accurate values by filtering out random temporal variations due to changes in weather conditions while significantly reducing speckle noise [53], [55]. With a time series of images at different times $\{t_1, t_2, \dots, t_M\}$, the arithmetic mean (AM) of 6-day coherence maps is calculated using

$$\overline{\rho_{vv}} = \frac{1}{M-1} \left(\sum_{t=1}^{M-1} \rho(z_t, z_{t+1}) \right). \quad (2)$$

Different objects have different properties in the temporal average time, for example, building areas and man-made structures have much higher coherence values, and forested and water areas have lower coherence values [54], [56]. As the forest develops and denser canopy is formed by age, the coherence values decrease. Together with the temporal average of repeat-pass coherences, the temporal average of the radar backscatter in both VV and VH channels and the ratio between them are calculated as follows:

$$\begin{aligned} \overline{\sigma_{vv}^0} &= \frac{1}{M} \sum_{t=1}^M \sigma_{vv}^0 \\ \overline{\sigma_{vh}^0} &= \frac{1}{M} \sum_{t=1}^M \sigma_{vh}^0 \\ \overline{R_{vhvv}} &= \frac{1}{M} \sum_{t=1}^M \frac{\sigma_{vh}^0}{\sigma_{vv}^0}. \end{aligned} \quad (3)$$

Following the steps described in this section, the AOI of each site was processed to generate the multitemporal coherence magnitude and backscatter intensity data. The geocoded S-1 products are used for the calculation of the aggregated images. The false color composite images of these products for the Romedal area in both ascending and descending orbits are shown in Fig. 2(a) and (b), where coherence over CCs and bare lands is significantly higher than over older forest classes characterized by higher radar backscatter intensity. A zoom-up area is shown in Fig. 2(d) together with a corresponding airborne orthophoto image in Fig. 2(f) covering the blue frame depicted in Fig. 2(a)–(c). This confirms higher repeat-pass coherence values and lower backscatter intensities over CC stands with yellow outlines and also slightly higher short-term repeat-pass coherence values over the REF stands with red outlines.

E. Sentinel-2 Data

The S-2 mission comprises a constellation of two polar-orbiting satellites placed in the same sun-synchronous orbit. It provides wide swath width (290 km) and high revisit time, 10 days at the equator with one satellite and 5 days with two satellites under the same viewing angles, which results in 2–3 days at mid-latitudes. At high latitudes, S-2 swaths overlap and some regions will be observed twice or more every 10 days, but with different viewing angles. However, we can only use summer images when the vegetation is developed, and we have sufficiently strong solar radiation to be able to utilize the spectral

TABLE II
CHOSEN SPECTRAL BANDS OF THE S-2

Sentinel-2 bands	Central wavelength (nm)	Res. (m)
Band 2-Blue	490.4	10
Band 4-Red	664.9	10
Band 5-Vegetation Red Edge	705.0	20
Band 6-Vegetation Red Edge	740.0	20
Band 7-Vegetation Red Edge	782.8	20
Band 8-NIR	842.0	10
Band 8A-Narrow NIR	865.0	20
Band 11-SWIR	1610.0	20
Band 12-SWIR	2190.0	20

properties. Clouds, however, are a common problem, and in practice, we can expect that by assembling cloudless pixels, we will be able to obtain one such cloud-free composite image per year. Both S-2 A and S-2B acquire 13 spectral bands in the visible, the near infrared (NIR), and the SWIR.

We selected a number of cloud-free S-2 datasets in level 2 A, where most bands were provided in 10×10 m spatial resolution. We resampled the 20 m bands to 10 m pixel spacing and reprojected onto the WGS-84 UTM coordinates. For Ås, we found two cloud free scenes in 2018, i.e., on 30th June and 5th July, and for Romedal, we found one cloud-free scene in 2016 (16th August) and two cloud-free scenes in 2018 (30th June, 5th July). The scenes were acquired from the 8th and 51st relative orbits. For each pixel, we extracted the median of the three values. This resulted in nine selected bands in Table II for each study area, all having 10 m resolution, and we partly used these bands as they were. The false color composite image of two spectral bands and the Normalized Difference Vegetation Index (NDVI) [57] for the Romedal area is shown in Fig. 2(c) with zoom-up area in Fig. 2(e), where CC stands represent higher SWIR and red-edge (REDG) values and lower NDVI values, and other forest stands are discriminated with larger NDVI values than elsewhere.

F. Modeling and Prediction

We carried out the classification of forest development and age classes with the RF classifier and the need for PCT in forest stands under regeneration with the RF regressor using the implementation provided by the *scikit-learn* package in the Python language.

1) *Random Forest (RF) Classification*: Decision tree classifiers have been known for a long time but they have shown problems related to overfitting and lack of generalization. The main idea behind RF is that it allows using high-dimensional and correlated data while minimizing the risk of overfitting [39], [40]. The RF classifier consists of many decision trees. To classify a new instance, each decision tree provides a classification for input data; RF collects the classifications and chooses the most voted prediction as the result. The input of each tree is a sampled data from the original dataset. In addition, a subset of features is randomly selected from the optional features to grow the tree at each node [58]. Essentially, the RF enables a large number of weak or weakly correlated classifiers to form a strong classifier.

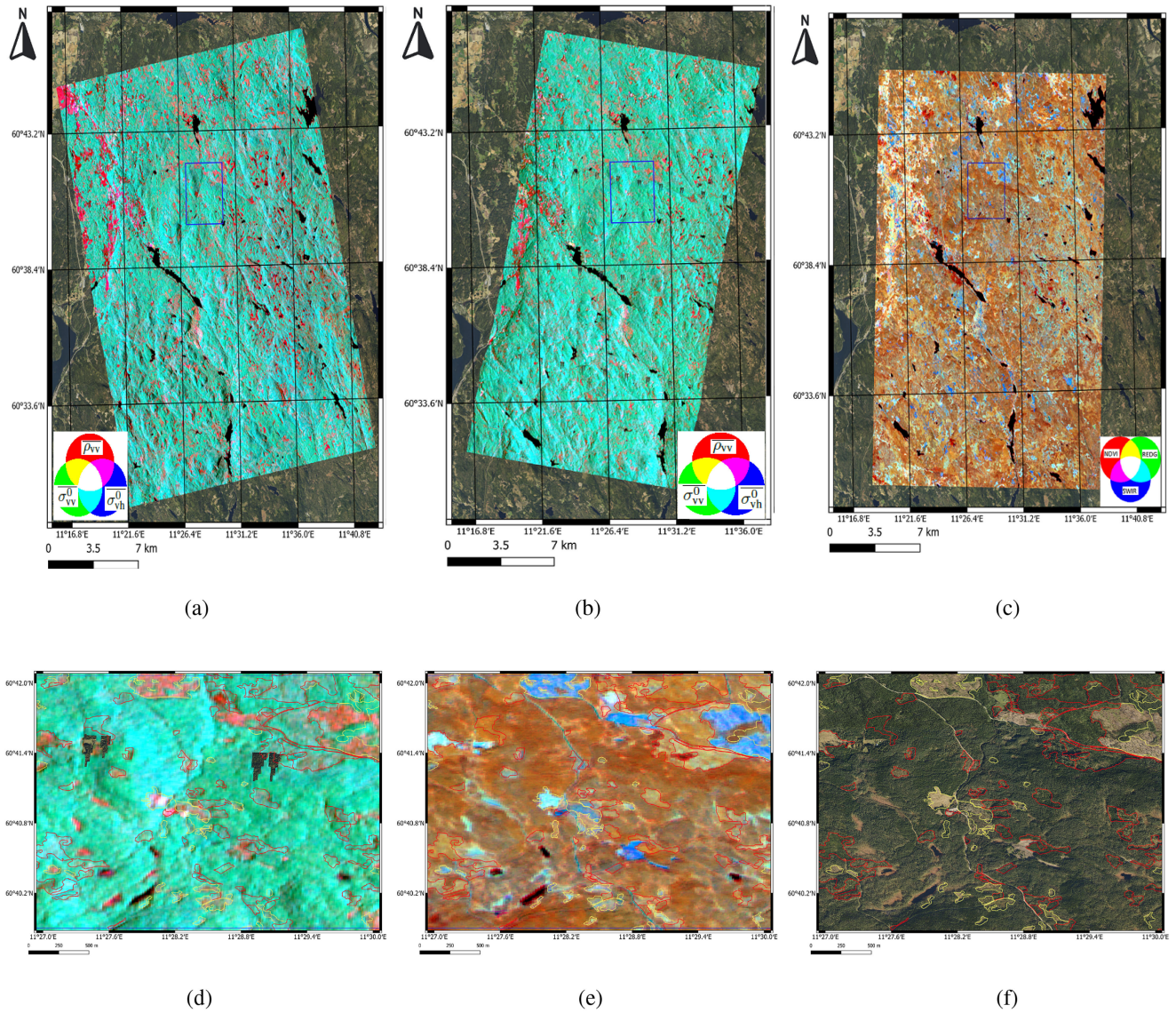


Fig. 2. (a) RGB composite of yearly average products of S-1 data in ascending orbit. (b) RGB composite of yearly average products of S-1 data in descending orbit. (c) RGB composite of median image of S-2 summer-time acquisitions (R: NDVI, G: REDG, B: SWIR). Bottom row shows the close-up of the area limited by the blue rectangle in the top row: (d) S-1, (e) S-2, and (f) airborne orthophoto image. The outlines of ground-truth REF and CC stands are shown in red and yellow, respectively. Outlines of other forest stands are not illustrated.

TABLE III
CHARACTERISTICS OF THE REFERENCE DATA SHOWING THE NUMBER OF TRAINING AND TESTING SAMPLES OF EACH FOREST AGE CLASS AND THE TOTAL NUMBERS

Forest type	Initial training set		Testing set		Total	
	Number of stands	Number of samples	Number of stands	Number of samples	Number of stands	Number of samples
Class I: CC	730	123,625	234	41,209	964	164,834
Class II: REF	2,062	550,367	679	183,456	2,741	733,823
Class III: YPF	3,009	694,812	995	231,603	4,004	926,415
Class IV: OPF	3,466	679,280	1,158	226,427	4,624	905,707
Class V: OF	1,492	264,890	524	88,297	2,016	353,187

The reference data of both test sites were first combined in order to cover a range of different growing conditions and were randomly split into two independent datasets at the stand level where 75% of the stands of each forest age class were selected for training the RF classification algorithm and the

remaining 25% of the stands were left for testing. This division of the original reference data is described in Table III. The resulting number of stands and, hence, the number of pixels of each forest age class, clearly varies among classes, showing that the training set is imbalanced. This can cause an overfitting toward the majority classes, which leads to reduced

classification accuracy for each individual class. To avoid this problem, the initial training set was subsampled so that all forest age classes had exactly the same number of training pixels.

Having trained the RF classification algorithm using the subsampled training data, the performance of the classification is presented in three cases: 1) S-1 variables; 2) S-2 variables; and 3) combination of both S-1 and S-2 variables. The evaluation is then performed over the whole set of testing data, which is formed by all pixels of the forest stands initially selected for testing (25% of the total stands). From the classification results obtained over the pixels in the testing data, the confusion matrix [59] is computed, which allows derivation of some metrics: recall, precision, and F-1 score [60] for each of the five forest age classes as well as the overall accuracy (OA) and Cohen's Kappa coefficient [61].

2) *RF Regression*: The aim of using the RF regression is to model the tree density and fraction of broadleaved trees in young forest stands under regeneration using S-1 and S-2 features. We estimated the stand density (number of trees per ha) and the fraction of broadleaved trees in the young stands under regeneration. We used field plots at the cluster level to train the RF between the input explanatory variables and the forest biophysical variables. We cross-validated the RF model at the cluster level using a leave-one-out cross-validation (LOOCV) technique [62]. The technique is run iteratively by removal of a single cluster and fitting a RF model on the remaining set of field clusters, and the prediction of the variables on the remaining observations. The cross-validated predictions are then utilized to calculate the coefficient of determination (R^2) and the root-mean-square error (RMSE) and its respective values as the percentage of the mean broadleaved fraction and mean tree density per ha.

III. RESULTS AND DISCUSSION

This section begins with a cross-correlation analysis of radar and optical variables for the target class in this study. Thereafter, the class separability between forest age classes for different radar and optical features is presented, followed by pixelwise classification results, ROC curves, and stand-level classification results. Finally, statistical analysis of the relationship between satellite parameters and forest inventory data is presented, and prediction maps of forest biophysical parameters and the PCT are shown. The workflow of the proposed methodology for detection of forest stands under regeneration in need of PCT is shown in Fig. 3.

A. Cross-Correlation Analysis of Radar and Optical Features

As discussed before, there are a number of variables and features derived from S-1 and S-2 that we test for forest age classification and young forest detection. This high dimensionality will significantly increase the training time of the machine learning model, it can make the model very complicated which in turn may lead to overfitting. Before using these features as inputs to the RF classification, we analyze the cross correlation between all pairs of the features listed below.

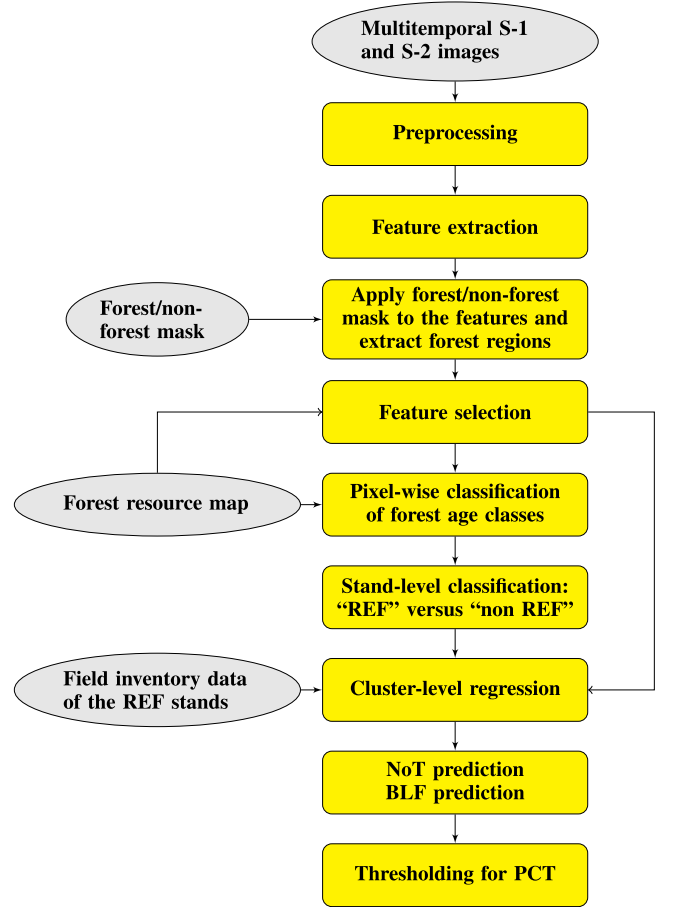


Fig. 3. Flowchart of the proposed method for young forest detection in this article, where NoT stands for the number of trees, and BLF stands for broadleaf fraction.

- 1) S-1 features from both ascending and descending orbits

$$\underline{\mathbf{X}}_1 = \left[\overline{\rho_{vv}}, \overline{\sigma_{vv}^0}, \overline{\sigma_{vh}^0}, \overline{R_{vhvv}} \right]_{Asc} \quad (4)$$

$$\underline{\mathbf{X}}_2 = \left[\overline{\rho_{vv}}, \overline{\sigma_{vv}^0}, \overline{\sigma_{vh}^0}, \overline{R_{vhvv}} \right]_{Dsc}$$

- 2) S-2 spectral bands

$$\underline{\mathbf{X}}_3 = [B02, B04, B05, B06, B07, B08, B11, B12, B8A] \quad (5)$$

The correlation coefficients between all pairs of S-1 and S-2 features for the REF ground-truth stands were calculated and are presented in the correlation matrices in Fig. 4. When there is a high correlation between two parameters, they show similar properties for the forest type. Highly correlated features decrease the training speed, decrease model interpretability, and, most importantly, decrease generalization performance on the test set. In case of low correlation, both features will contribute to the improvement of the REF discrimination. As in Fig. 4, all correlations marked red and blue represent high and low correlations, respectively. For example, normalized backscatter coefficients of both the VV and VH channels represent high

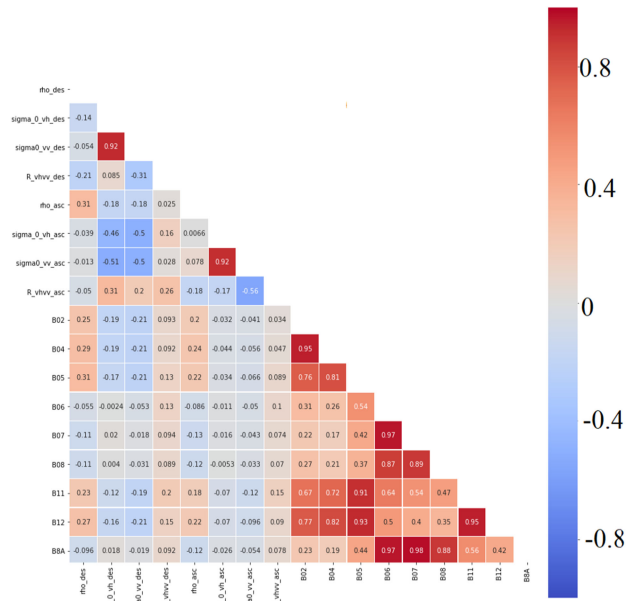


Fig. 4. Cross-correlation matrix between all pairs of S-1 and S-2 features from the REF ground-truth pixels.

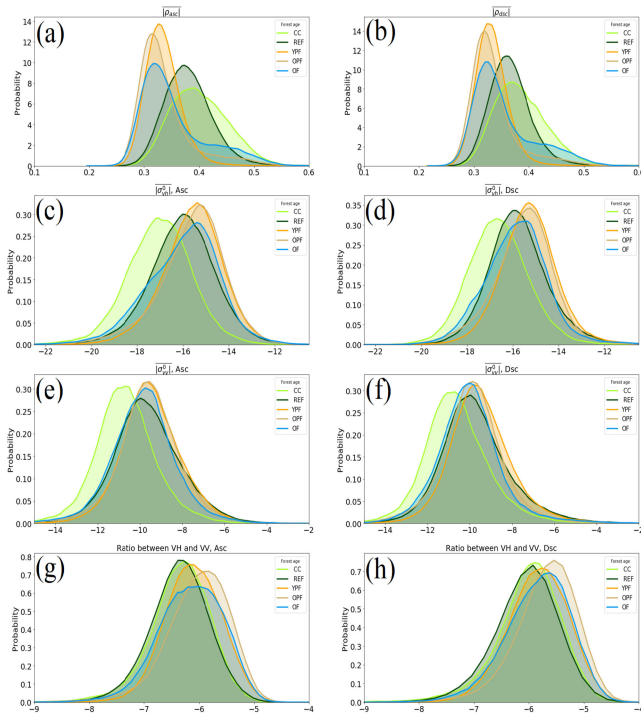


Fig. 5. Distributions of different forest age classes for different parameters of S-1 data. The curves of the target class, i.e., REF, are shown in dark green.

correlation. There are high correlations between optical bands 6, 7, 8, and 8 A, and also between bands 11 and 12.

B. Distribution Separability

To assess the separability of forest age classes with S-1 and S-2 data, we first looked at the distribution of different optical and radar features within each class at the pixel level. Fig. 5

shows the distribution of the annual mean of the 6-day repeat-pass coherence magnitude, backscatter intensity in VV and VH as well as the ratio between channels between ascending and descending orbits, per forest age class. We have chosen to show the distributions of temporal mean rather than the unaggregated data to yield more pronounced differences between classes as well as mitigate the underlying variability in the SAR variables either due to noise, seasonality, or other effects. Fig. 5(a) and (b) represents the yearly average 6-day coherence magnitude distributions of ground-truth forest stands for both ascending and descending tracks, where the REF shown in the dark green curve represents slightly higher mean coherence than the other forest age classes, which is to be expected because in young forests there are less volume scattering effects and a lesser fraction of the radar energy is backscattered from trees under generation. It is also clear that the CC class represents high repeat-pass coherence magnitude and is well separated from the other forest age classes. The other forest classes are found to the left of these two classes, which is expected due to higher vegetation density and tree height with respect to the REF class. It is shown in Fig. 5(c) and (d) that for CC stands shown in the light green curve, the radar backscatter is mostly lower than the other classes. The reason for this is that volume scattering within the tree canopies of the older forest stands is higher than in the younger forest stands and grassy CCs. For the REF class, its curve is skewed more to the left and forest in the regeneration phase has produced lower backscatter compared to the other forest classes, whereas the backscatter values of the older forest types are larger. As in Fig. 5(e)–(h), similar signatures for forest stands in the VV channel and the ratio between VH and VV were extracted.

The distributions of different forest classes for S-2 bands are shown in Fig. 6. Looking at the curves of S-2 spectral bands confirms that the REF produces greater reflectance than the other forest classes. This is because the forest reflectance generally decreases with the age and height of trees. During the early growth stage of young forest stands, the satellite signal is mainly dominated by the reflectance of the ground vegetation, exposed soil, or land. As forest biomass increases, the reflectance properties and total leaf area of the canopy becomes more dominant than the ground vegetation. It is evident in Fig. 6(c)–(h) that the reflectance of the REDG, NIR, and SWIR bands from the REF is greater than that of the other forest classes. The greater reflectance of the REF with respect to other forest classes in the SWIR band is probably an effect of the growing trees and the shadows they cause [5].

Spectral VIs are commonly used in addition to spectral bands as the input of the supervised classification system in remote sensing literature. More specifically, we also computed the four commonly used VIs from S-2 spectral bands for the separability analysis: the NDVI, the enhanced vegetation index (EVI) [63], the moisture stress index (MSI) [64], and the normalized difference moisture index (NDMI) [65]. The probability distributions of the forest age classes for these VIs are shown in Fig. 7. It is evident that there is a good separation between the CC class and the other forest age classes, whereas the REF class overlaps

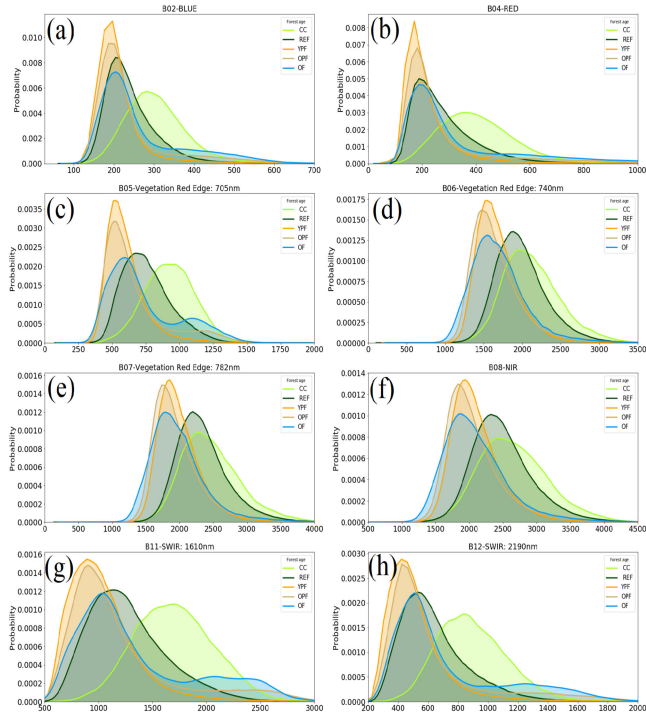


Fig. 6. Distributions of different forest age classes for different parameters of S-2 data. The curves of the target class, i.e., REF, are shown in dark green.

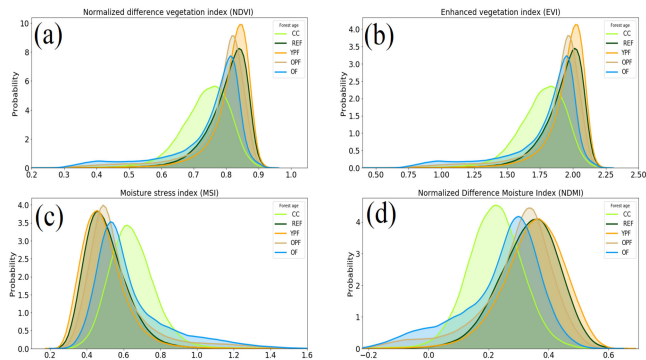


Fig. 7. Distributions of different forest age classes for the four vegetation indices: NDVI, EVI, MSI, and NDMI.

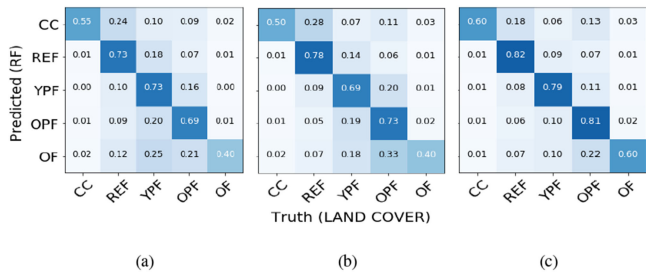


Fig. 8. RF confusion matrix for forest-type mapping and discrimination, where CC = Clear Cut; REF = Regenerated Forest (target class); YPF= Young Production Forest; OPF = Older Production Forest; and OF= Old Forest. (a) S-1. (b) S-2. (c) S-1 and S-2.

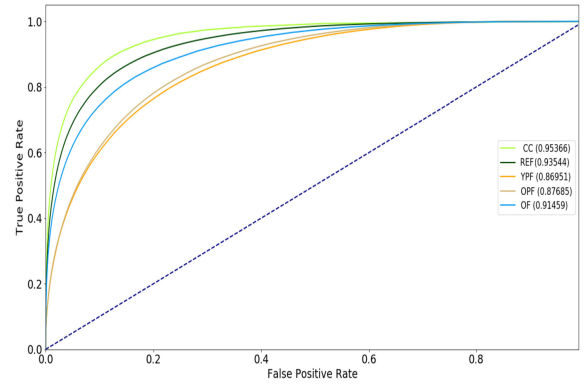


Fig. 9. ROC curves of the RF classifier, represented as “one versus rest” for each forest class in the dataset. Numbers in brackets are the AUC values. The ROC curve of the target class, i.e., REF, is shown in dark green.

with other classes and a separation between the REF and the older forest classes is not possible based on the VIs.

C. Pixelwise Classification of Forest Age Classes

The input features for classification in this research include the S-2 spectral bands, VIs, S-1 backscattering coefficients, and repeat-pass coherence in both ascending and descending orbits. Often in a high-dimensional feature set, there remain several features which are redundant meaning these features are nothing but extensions of the other essential features. These redundant features do not effectively contribute to the model training as well. So, clearly, there is a need to extract the most important and the most relevant features for a dataset in order to get the most effective predictive performance. We selected the most important variables based on the cross-correlation analysis, class separability, and the features’ importance ranked by the RF method. By doing this, the data redundancy and computation load can be effectively reduced. We selected the following features for the RF classifier:

- the annual average of the backscatter intensity time series of the VH channel in both ascending and descending orbits;
- the annual average of the InSAR coherence magnitude time series of the VV channel in both ascending and descending orbits;
- the median value of REDG (B06) of the selected acquisitions; and
- the median value of SWIR (B11) of the selected acquisitions.

Fig. 10(a) shows a ground truth map of forest stands in the Romedal site for the close-up area in Fig. 2 that were to be visually inspected for the experiments. The forest-stand classification results are shown in this section, and the performance of the classification is presented in three alternatives; 1) S-1 variables, 2) S-2 variables, and 3) combination of both S-1 and S-2 variables. The performance of the classification in three cases is assessed by comparing with the ground truth obtained from the forest resource map. The confusion matrix [59] is obtained by combining data from both test sites. Fig. 8 provides such a confusion matrix obtained for all three cases. One can see that most classes are identified accurately. In particular, the REF

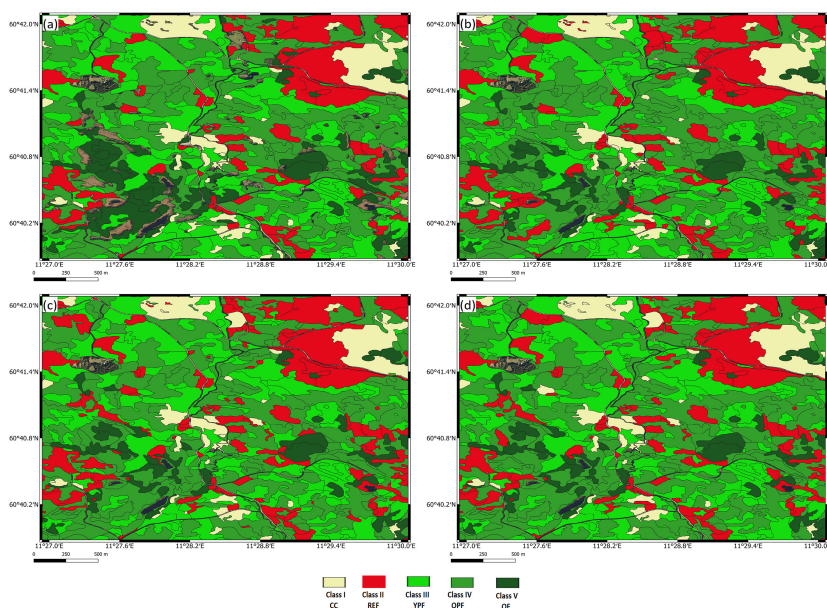


Fig. 10. Comparison of S-1 and S-2 input features for stand-level classification in the Romedal site with five classes based on the RF classification strategy. The REF as the target class is illustrated in red and the other forest age classes in other colors. (a) Ground-truth map of forest age classes and classification maps of a close-up area in Romedal in three cases. (b) S-1 features. (c) S-2 features. (d) Combination of S-1 and S-2 features.

TABLE IV
PIXELWISE CLASSIFICATION RESULTS OF TEST SITES IN ÅS AND ROMEDAL FROM: (TOP) S-1 FEATURES; (MIDDLE) S-2 BANDS; AND (BOTTOM) COMBINATION OF S-1 AND S-2 FEATURES

S-1			
Class	Recall (%)	Precision (%)	F-1 (%)
CC	50.5	77.0	61.0
REF	76.8	66.0	71.0
YPF	69.3	65.1	67.1
OPF	70.6	67.5	69.0
OF	38.5	82.6	52.5
OA: 67.6% F1-score: 67.0%, and Kappa coeff.: 0.56			
S-2			
Class	Recall (%)	Precision (%)	F-1 (%)
CC	46.1	73.3	56.6
REF	78.8	74.0	76.3
YPF	67.8	66.0	67.3
OPF	74.0	65.1	69.3
OF	41.0	79.9	54.2
OA: 68.8% F1-score: 68.2%, and Kappa coeff.: 0.57			
S-1 & S-2			
Class	Recall (%)	Precision (%)	F-1 (%)
*CC	81.7	68.5	58.9
*REF	76.2	79.2	82.4
*YPF	77.9	78.3	78.8
*OPF	74.9	78.0	81.4
*OF	87.4	69.2	57.3
OA: 77.3% F1-score: 77.0%, and Kappa coeff.: 0.69			

as a target class in this study is detected with detection rates over 70%. The reason for the detection rate for the CC class might be the mismatch between the year of ground-truth data and that of the satellite data. It might be that some of the OF had been harvested between the collection of ground-truth data and satellite observations. The recall, precision, and F-1 score for each forest class are listed in Table IV. Regarding the use of only S-1 variables, the results of this study indicate that the interferometric coherence is a formidable source of information

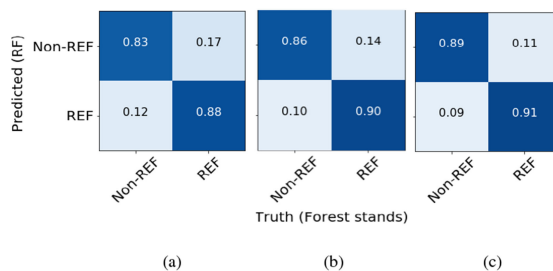


Fig. 11. RF confusion matrix for young forest detection. Where REF = Regenerated Forest versus the other forest stands. The result is obtained on combined data from both the Ås and Romedal study sites. (a) S-1. (b) S-2. (c) S-1 and S-2.

TABLE V
STAND-LEVEL CLASSIFICATION RESULTS OF TEST SITES IN ÅS AND ROMEDAL FROM: (TOP) S-1 FEATURES; (MIDDLE) S-2 BANDS; AND (BOTTOM) COMBINATION OF S-1 AND S-2 FEATURES

S-1			
Class	Recall (%)	Precision (%)	F-1 (%)
Non-REF	83.0	97.3	89.6
REF	88.2	50.3	64.0
OA: 83.8% F1-score: 85.4%, and Kappa coeff.: 0.55			
S-2			
Class	Recall (%)	Precision (%)	F-1 (%)
Non-REF	86.1	97.9	91.6
REF	90.5	56.1	69.2
OA: 86.9% F1-score: 88.0%, and Kappa coeff.: 0.61			
S-1 & S-2			
Class	Recall (%)	Precision (%)	F-1 (%)
Non-REF	88.7	98.1	93.2
REF	91.2	61.2	73.2
OA: 89.1% F1-score: 89.9%, and Kappa coeff.: 0.67			

for forest resource mapping, having produced an OA of over 75%. It should be highlighted that 6-day InSAR coherence magnitude is shown to perform better than backscatter intensity

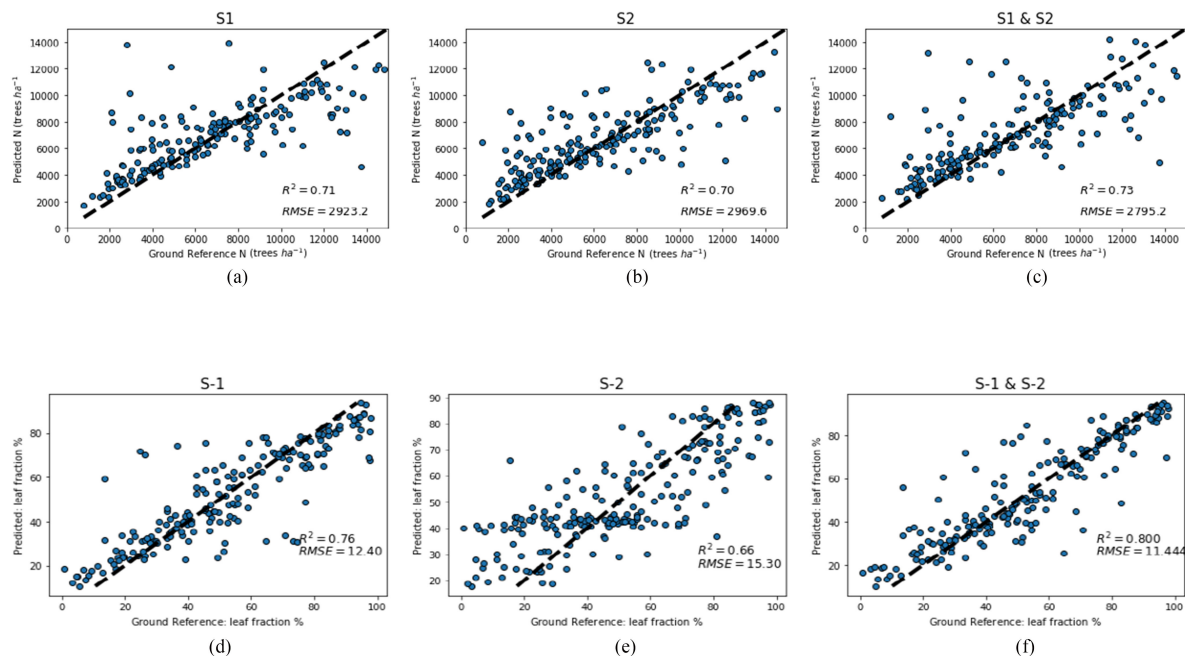


Fig. 12. Scatterplots of predicted (y -axis) versus the ground reference values (x -axis) at the cluster level for the biophysical variables: stand density (upper row) and broadleaf fraction (lower row) based on the RF regression analysis for three alternatives: S-1, S-2, and S-1 and S-2. Each point corresponds to a forest cluster of 250 m^2 . The variables include the broadleaf fraction in percentage and tree density (N ; trees ha^{-1}). The error metrics (both RMSE and statistical R^2 measure) are also shown.

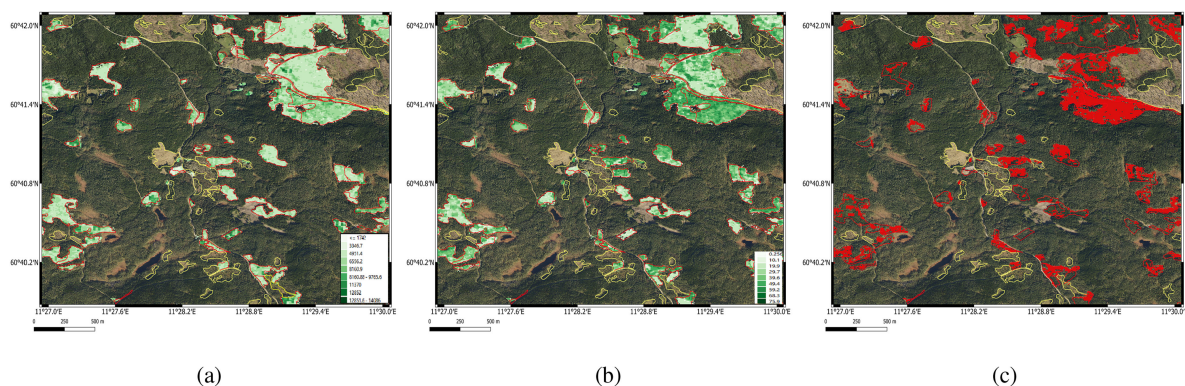


Fig. 13. Prediction maps of: (Left) the number of trees ha^{-1} ; (Middle) the broadleaf fraction; (Right) the need for PCT.

for forest age classification, although this analysis has shown that it is beneficial to include both backscatter intensity and coherence magnitude as both observables are complementary, improving accuracy of results when both are combined. A different sensitivity of S-2 spectral bands for forest age classification has been observed. The SWIR, in particular, has shown a good potential to discriminate between the REF, older forest stands, and CCs. The combination of both S-1 and S-2 proves to be complementary.

D. ROC Curve

Machine learning classifiers predict the class labels with a certain confidence, but the threshold for the prediction of a certain label can be set by the user depending on tuning parameters in the

classifier. The receiver operating characteristic (ROC) curve [66] shows the diagnostic ability of a classifier as its discrimination threshold is varied. Usually, it is shown for a binary system, but it can also be used in multiclass classifications, where it calculates the “one versus the rest” characteristics for each represented class. The horizontal axis shows the false positive rate and the vertical axis shows the true positive rate at different steps. Good classifier performance is characterized by a curve, which has a large integral value, also known as the area under curve (AUC). There are usually multiple classes in the remote sensing images, and we suppose that all of them are divided into two classes, namely, target class and nontarget class. Target class is the one to be evaluated, while the remaining classes are considered to be of nontarget class. Then the classification of multiple classes

was converted to binary classification, and consequently the ROC curve could be obtained. In this study, the ROC curve was derived for each forest age class, from which AUC was derived to evaluate the performance of the RF classifier. ROC curves for each forest class with the corresponding AUC are shown in Fig. 9. The performance of the RF classifier is varied for different forest classes. To be specific, the best performance of the RF was for CCs and the target class, i.e., REF.

E. Stand-Level Classification of Forest Age Classes

In this study, we classify forest stands rather than single pixels. The rationale for this is partly that foresters use stands as the unit in their management, and do not need forest data with a higher spatial resolution and partly because we in this way reduce random noise in the data by aggregating variables to larger spatial units. Using outlines of forest stands from the forest resource map, we aggregated the pixel-based classification maps to the stand level for testing performance of the RF classification. Since the aim of this article is detection of forest stands under regeneration, we grouped non-REF classes as a single class in the analysis so that we had only two classes for the final validation: REF versus the other forest stands. We then evaluated the accuracy of the REF detection results. Fig. 10 (b)–(d) shows stand-level classification results for a close-up area in Fig. 2. The confusion matrix of the REF versus the other forest classes is shown in Fig. 11 for all three alternatives. It is clear that in all cases, we are able to detect REF stands with high accuracy. The recall, precision, and F-1 score for the target class (REF) versus other forest stands are reported in Table V. Pixelwise classification accuracy using SAR bands alone was around 67.6% for the five forest age classes. When non-REF classes were merged into a single class, the classification accuracy increased to around 83.8%. A dataset comprising SAR and optical bands showed increased classification accuracy in relation to SAR data alone. Following merging of non-REF classes, the OA was around 89.1%.

F. Statistical Analysis of the Relationship Between Retrieval Satellite Variables and Forest Inventory Data

In this section, we model the biophysical parameters of stands under regeneration using satellite and field-inventory data and decide for tending/PCT based on prediction maps. For analysis of correlation between the S-1 and S-2 variables and forest properties, we used the RF regression for modeling tree density and broadleaf fraction in the REF stands. These variables were obtained from 50 m² circle-shaped plots in the field inventory data. We modeled the forest parameters in the cluster level, which are taken from the average of every five plots inside a cluster. We found that a sample of one plot of five clusters may not be sufficient to estimate the biophysical parameters as in this study. The results of the correlation analysis indicate that the biophysical parameters of the forest stands under regeneration are highly correlated with the S-1 and S-2 features. Prediction of the broadleaf fraction and tree density was obtained with higher coefficients of determination R^2 , and lower RMSE when using both S-1 and S-2 than S-1 and S-2 variables alone. The results of the correlation analysis are plotted in Fig. 12.

G. Prediction Maps of the Number of Trees, Broadleaf Fraction, and PCT

After modeling the biophysical parameters with a trained RF regression obtained from the field inventory and satellite data, we used this model for prediction of the number of trees and broadleaf fraction at each pixel. Fig. 13(a) and (b) shows the prediction maps of the number of trees and broadleaf fraction, respectively. These maps were then used to decide on PCT with the given thresholds. In this study, we performed thresholding of pixels above 2500 trees per ha and 30% broadleaf fraction. Fig. 13(c) shows the PCT maps where red pixels represent the areas in need of PCT.

IV. CONCLUSION

In this research, we analyzed and demonstrated the value of multitemporal S-1 and S-2 for characterization and mapping of young forests under regeneration in two study sites from southeastern Norway. The main aim was to test the SAR and optical features to discriminate forest stands under regeneration from other forest stands. In general, the separability of forest stands under regeneration from other stands can be dependent on the study site. A larger selection of study sites may be required to determine whether this is due to the characteristics of the individual study sites and forest types found in each site. The transferability of the approach for detection of forest stands under regeneration using time-series of remotely sensed data and , however, is challenged by the lack of samples used to train the supervised algorithm, especially for inaccessible steep mountainous areas and change in phenological cycles caused by climate variations in a mountainous area.

We first extracted multitemporal radar backscattering coefficients (VV/VH) and 6-day repeat-pass coherence magnitudes in the VV channel from S-1 SLC products for both ascending and descending orbits. We then applied temporal averaging of these products to mitigate variations in backscatter and coherence values not attributable to land cover, such as topography, seasonality, and random fluctuations. It is expected that denser forest exhibits less annual variability in backscatter compared to a growing forest or bare soil. This may be explained by two factors. First, large biomass values are likely to be above the saturation point for biomass-backscatter relationships, and second, the emitted radar signal is unlikely to reach the soil through dense canopies, and differences in soil moisture and roughness will not change the backscatter [24], [54]. We will consider using the standard deviation of all available S-1 variables as a new feature set in the RF classification algorithm in our future work. We also derived the S-2 spectral bands and VIs of cloud-free composite images in summer to be fused with the S-1 features.

We provided a systematic investigation of S-1 parameters and S-2 spectral bands for the specific purpose of discrimination between forest stands under regeneration versus the other forest age classes using class separability, cross-correlation analysis, and the features' importance ranked by the RF approach. We found that the most powerful S-1 features were first the repeat-pass coherence and second the radar backscatter intensity of the VH channel. For the S-2 spectral bands, we found that the NIR, SWIR, and REDG channels presented a good separability

between the REF class and the other classes, but having high correlation between some parameters in the cross-correlation analysis of the REF class, we ended up choosing the REDG (B06) and SWIR (B11) bands as inputs of the RF classification. The use of spectral VIs did not provide a good separation between the REF and the other classes.

We used the most important features chosen in the previous step to train the classical RF classification algorithm. We did a comparative study of performance of the algorithm in three cases: 1) using only S-1 features; 2) using only S-2 optical bands; and 3) using combination of S-1 and S-2 features. For the purpose of discrimination of the REF stands, the use of six chosen S-1 and S-2 features was seen to perform at least as well as all features, i.e., all S-1 and S-2 parameters. This indicates that the selected features not only contain sufficient information for the purpose investigated here but also reduce the computational cost of the training and prediction steps of the supervised machine learning algorithm. Regarding the use of only S-1 variables, the classification results of this study indicated that the 6-day interferometric coherence was shown to perform better than the backscatter intensity for forest age classification, although this analysis showed that it is beneficial to include both backscatter intensity and coherence. We showed that the S-2 spectral features provided slightly better accuracies than the S-1 variables for discrimination of the REF, old forest stands, and CCs, and a combination of S-1 and S-2 parameters yielded the best results. We used the RF regression for the analysis of correlation between the S-1 and S-2 variables and forest properties in forest stands under regeneration, and we estimated tree density and broadleaf fraction in the cluster level with coefficient of determination (R^2) of about 0.70 and 0.80, respectively. The cluster-level RMSE of the tree density and broadleaf fraction were about 2795 trees ha^{-1} and 11.44%, respectively. Model accuracy improved at the cluster-level scale (250 m^2) as compared to the plot-level scale (50 m^2).

To conclude, this study has shown that time series data of both S-1 and S-2 will make a useful contribution to discriminating forest stands under regeneration from other stands, and also to finding forest stands in need of PCT. More accurate classification of forest stands under regeneration in boreal areas has a significant practical value in supporting the effective management and protection of forest resources.

ACKNOWLEDGMENT

Sentinel data are provided free of charge by the European Union Copernicus program. The collection of field inventory data was carried out by Norskog. The authors would also like to thank the reviewers for their useful comments and suggestions that help to improve this article.

REFERENCES

- [1] S. Puliti, S. Solberg, and A. Granhus, "Use of UAV photogrammetric data for estimation of biophysical properties in forest stands under regeneration," *Remote Sens.*, vol. 11, no. 3, 2019, Art. no. 233.
- [2] G. Sjøgaard *et al.*, "Forest management for value production in a changing climate," (in Norwegian). *NIBIO Rapport 3/99/2017*. Ås, Norway.
- [3] *Skogselskapet* "Precommercial thinning has low cost but large benefits," (in Norwegian), 2021. Accessed: Dec. 2019. [Online]. Available: <https://www.skogselskapet.no/skogeierguiden-2-ungskogpleie-koster-lite-men-gir-mye/Web-page>
- [4] T. Øvergård, "Ungskogpleie [Precommercial thinning]," (in Norwegian). *Tech. Rep. Skogbrukets Kursinstitutt*, Gjøvik, Norway, Oct. 2018.
- [5] H. Olsson, "A method for using Landsat time series for monitoring young plantations in boreal forests," *Int. J. Remote Sens.*, vol. 30, no. 19, pp. 5117–5131, 2009.
- [6] D. O. J. Reventlow, T. Nord-Larsen, and J. P. Skovsgaard, "Pre-commercial thinning in naturally regenerated stands of European beech (*Fagus sylvatica* L.): Effects of thinning pattern, stand density and pruning on tree growth and stem quality," *Forestry: An Int. J. Forest Res.*, vol. 92, no. 1, pp. 120–132, 2018.
- [7] S. Puliti *et al.*, "Modelling above-ground biomass stock over Norway using national forest inventory data with ArcticDEM and Sentinel-2 data," *Remote Sens. Environ.*, vol. 236, 2020, Art. no. 111501.
- [8] M. Berger, J. Moreno, J. A. Johannessen, P. F. Levelt, and R. F. Hanssen, "ESA's sentinel missions in support of earth system science," *Remote Sens. Environ.*, vol. 120, pp. 84 – 90, 2012.
- [9] *Earth Observation Satellites*. Accessed: Sep. 2019. [Online]. Available: <https://www.copernicus.eu/en/about-copernicus/infrastructure/satellites-component> September 2019
- [10] E. Grabska, P. Hostert, D. Pflugmacher, and K. Ostapowicz, "Forest stand species mapping using the Sentinel-2 time series," *Remote Sens.*, vol. 11, no. 10, 2019, Art. no. 1197.
- [11] P. Addabbo, M. Focareta, S. Marcuccio, C. Votto, and S. Ullo, "Contribution of Sentinel-2 data for applications in vegetation monitoring," *ACTA IMEKO*, vol. 5, no. 2, pp. 44–54, Sep. 2016.
- [12] P. Rajah, J. Odindi, O. Mutanga, and Z. Kiala, "The utility of Sentinel-2 vegetation indices (VIs) and Sentinel-1 synthetic aperture radar (SAR) for invasive alien species detection and mapping," *Nat. Conservation*, vol. 35, pp. 41–61, Jun. 2019.
- [13] E. S. Kasischke, J. M. Melack, and M. C. Dobson, "The use of imaging radars for ecological applications—A review," *Remote Sens. Environ.*, vol. 59, no. 2, pp. 141–156, Feb. 1997.
- [14] B. Koch, "Status and future of laser scanning, synthetic aperture radar and hyperspectral remote sensing data for forest biomass assessment," *ISPRS J. Photogramm. Remote Sens.*, vol. 65, no. 6, pp. 581–590, 2010.
- [15] T. Le Toan, A. Beaudoin, J. Riou, and D. Guyon, "Relating forest biomass to SAR data," *IEEE Trans. Geosci. Remote Sens.*, vol. 30, no. 2, pp. 403–411, Mar. 1992.
- [16] M. C. Dobson, F. T. Ulaby, T. LeToan, A. Beaudoin, E. S. Kasischke, and N. Christensen, "Dependence of radar backscatter on coniferous forest biomass," *IEEE Trans. Geosci. Remote Sens.*, vol. 30, no. 2, pp. 412–415, Mar. 1992.
- [17] S. Saatchi, "Mapping tropical forest biomass: Synthesis of ground and remote sensing inventory," The High Carbon Stock Science Study, Tech. Rep. 2015.
- [18] D. Small, "Flattening gamma: Radiometric terrain correction for SAR imagery," *IEEE Trans. Geosci. Remote Sens.*, vol. 49, no. 8, pp. 3081–3093, Aug. 2011.
- [19] V. Akbari, A. Doulgeris, and T. Eltoft, "Monitoring glacier changes using multitemporal multipolarization SAR images," *IEEE Trans. Geosci. Remote Sens.*, vol. 52, no. 6, pp. 3729–3741, Jun. 2014.
- [20] R. Ahmed, P. Siqueira, S. Hensley, B. Chapman, and K. Bergen, "A survey of temporal decorrelation from spaceborne L-band repeat-pass InSAR," *Remote Sens. Environ.*, vol. 115, no. 11, pp. 2887–2896, 2011.
- [21] F. Sica, A. Pulella, M. Nannini, M. Pinheiro, and P. Rizzoli, "Repeat-pass SAR interferometry for land cover classification: A methodology using Sentinel-1 short-time-series," *Remote Sens. Environ.*, vol. 232, 2019, Art. no. 111277.
- [22] A. W. Jacob *et al.*, "Sentinel-1 InSAR coherence for land cover mapping: A comparison of multiple feature-based classifiers," *IEEE J. Sel. Topics Appl. Earth Observ. Remote Sens.*, vol. 13, pp. 535–552, Jan. 2020.
- [23] N. Pinto, M. Simard, and R. Dubayah, "Using InSAR coherence to map stand age in a boreal forest," *Remote Sens.*, vol. 5, pp. 42–56, 2012.
- [24] S. Quegan, T. Le Toan, J. J. Yu, F. Ribbes, and N. Floury, "Multitemporal ERS SAR analysis applied to forest mapping," *IEEE Trans. Geosci. Remote Sens.*, vol. 38, no. 2, pp. 741–753, Mar. 2000.

- [25] W. A. Salas, M. J. Ducey, E. Rignot, and D. Skole, "Assessment of JERS-1 SAR for monitoring secondary vegetation in Amazonia: I spatial and temporal variability in backscatter across a chrono-sequence of secondary vegetation stands in Rondonia," *Int. J. Remote Sens.*, vol. 23, no. 7, pp. 1357–1379, 2002.
- [26] E. Rignot, W. A. Salas, and D. L. Skole, "Mapping deforestation and secondary growth in Rondonia, Brazil, using imaging radar and thematic mapper data," *Remote Sens. Environ.*, vol. 59, no. 2, pp. 167–179, 1997.
- [27] T. M. Kuplich, "Classifying regenerating forest stages in Amazonia using remotely sensed images and a neural network," *Forest Ecol. Manage.*, vol. 234, no. 1, pp. 1–9, 2006.
- [28] J. Pulliainen, K. J. M. Heiska, J. Hyypää, and M. Hallikainen, "Backscattering properties of boreal forests at the c- and x-bands," *IEEE Trans. Geosci. Remote Sens.*, vol. 32, no. 5, pp. 1041–1050, Sep. 1994.
- [29] N. Ackermann, C. Thiel, M. Borgeaud, and C. Schmillius, "Cometric coherence signatures over Germany's low mountain range forested areas," in *Proc. IEEE Int. Geosci. Remote Sens. Symp.*, 2012, pp. 5514–5517.
- [30] W. Wagner *et al.*, "Large-scale mapping of boreal forest in Siberia using ERS tandem coherence and JERS backscatter data," *Remote Sens. Environ.*, vol. 85, no. 2, pp. 125–144, 2003.
- [31] V. Akbari and S. Solberg, "Clear-cut detection and mapping using Sentinel-1 backscatter coefficient and short-term interferometric coherence time series," *IEEE Geosci. Remote Sens. Lett.*, to be published.
- [32] Akbari Vahid, G. Picard and Solberg Svein, "Clear-Cut Detection and Mapping Using Sentinel-1 Backscatter Coefficient and Short-Term Interferometric Coherence Time Series," *IEEE Geoscience and Remote Sensing Letters*, vol. 475, Jan. 2020, pp. 1–5, doi: [10.1109/LGRS.2020.3039875](https://doi.org/10.1109/LGRS.2020.3039875)
- [33] M. E. Engdahl and J. M. Hyypää, "Land-cover classification using multitemporal ERS-1/2 InSAR data," *IEEE Trans. Geosci. Remote Sens.*, vol. 41, no. 7, pp. 1620–1628, Jul. 2003.
- [34] M. Engdahl, "Multitemporal InSAR in land-cover and vegetation mapping," Ph.D. dissertation, Aalto University, Espoo, Finland, 2013.
- [35] J. Pulliainen, M. Engdahl, and M. Hallikainen, "Feasibility of multitemporal interferometric SAR data for stand-level estimation of boreal forest stem volume," *Remote Sens. Environ.*, vol. 85, no. 4, pp. 397–409, 2003.
- [36] M. Santoro, J. Askne, G. Smith, and J. E. Fransson, "Stem volume retrieval in boreal forests from ERS-1/2 interferometry," *Remote Sens. Environ.*, vol. 81, no. 1, pp. 19–35, 2002.
- [37] T. Nilson and U. Peterson, "Age dependence of forest reflectance: Analysis of main driving factors," *Remote Sens. Environ.*, vol. 48, no. 3, pp. 319–331, 1994.
- [38] T. Nilson and U. Peterson, "A forest canopy reflectance model and a test case," *Remote Sens. Environ.*, vol. 37, no. 2, pp. 131–142, 1991.
- [39] L. Breiman, "Random forests," *Mach. Learn.*, vol. 45, no. 1, pp. 5–32, Oct. 2001.
- [40] K. T. Ho, "The random subspace method for constructing decision forests," *IEEE Trans. Pattern Anal. Mach. Intell.*, vol. 20, no. 8, pp. 832–844, Aug. 1998.
- [41] Y. Liu, W. Gong, X. Hu, and J. Gong, "Forest type identification with random forest using Sentinel-1 A, Sentinel-2 A, multi-temporal Landsat-8 and DEM data," *Remote Sens.*, vol. 10, no. 6, 2018, Art. no. 946.
- [42] K. P. Bennett and C. Campbell, "Support vector machines: Hype or hallelujah?," *SIGKDD Explorations Newsl.*, vol. 2, no. 2, pp. 1–13, Dec. 2000.
- [43] N. S. Altman, "An introduction to kernel and nearest-neighbor nonparametric regression," *Amer. Statistician*, vol. 46, no. 3, pp. 175–185, 1992.
- [44] M. Hansen, P. Potapov, B. Margono, S. Stehman, S. Turubanova, and A. Tyukavina, "High-resolution global maps of 21st-century forest cover change," *Science*, vol. 344, no. 6187, May 2014, Art. no. 981.
- [45] K. O. Viken, "National Forest Inventory field guide 2018," *NIBIO BOK*, 4 (6).
- [46] J. Breidenbach, A. Granhus, G. Hylen, R. Eriksen, and R. Astrup, "A century of national forest inventory in Norway-informing past, present, and future decisions," vol. 7, May 2020 Art. no. 46.
- [47] H. Braastad, "Tilvekstmodellprogram for bjørk," Norwegian Forest Research Institute, Tech. Rep. 1/77, Ås, Norway, 1977.
- [48] B. Tveite, "Site-index curves for Norway spruce (*Picea abies* (L.) Karst)," (in Norwegian), *Meddelelser fra Norsk Institutt for Skogforskning*, Tech. Rep. 33, Ås, Norway, vol. 33, no. 1, pp. 1–48., 1977.
- [49] F. D. Zan and A. M. Guarnieri, "TOPSAR: Terrain observation by progressive scans," *IEEE Trans. Geosci. Remote Sens.*, vol. 44, no. 9, pp. 2352–2360, Sep. 2006.
- [50] Q. Yuxiao, "Sentinel-1 wide swath interferometry: Processing techniques and applications," Ph.D. dissertation, Uni. Purdue, West Lafayette, IN, USA, Dec. 2018.
- [51] R. Touzi, A. Lopes, J. Bruniquel, and P. W. Vachon, "Coherence estimation for SAR imagery," *IEEE Trans. Geosci. Remote Sens.*, vol. 37, no. 1, pp. 135–149, Jan. 1999.
- [52] M. Fomelis *et al.*, "Esa SNAP-StaMPS integrated processing for Sentinel-1 persistent scatterer interferometry," in *Proc. IEEE Int. Geosci. Remote Sens. Symp.*, 2018, pp. 1364–1367.
- [53] C. Oliver and S. Quegan, *Understanding Synthetic Aperture Radar Images*, 2nd ed. Raleigh, NC, USA: SciTech Publishing, 2004.
- [54] J. N. Hansen, E. T. A. Mitchard, and S. King, "Assessing forest/non-forest separability using Sentinel-1 c-band synthetic aperture radar," *Remote Sens.*, vol. 12, no. 11, 2020, Art. no. 1899.
- [55] V. Akbari, "Multitemporal analysis of multipolarization synthetic aperture radar images for robust surface change detection," Ph.D. dissertation, Uni. Tromsø, Tromsø, Norway, Jun. 2013.
- [56] T. Nikaein, V. Akbari, and H. Arefi, "Added value of multitemporal polarimetric UAVSAR data for permanent scatterers detection," in *Proc. IEEE Int. Geosci. Remote Sens. Symp.*, Jul. 2018, pp. 5666–5669.
- [57] J. Rouse, R. Haas, J. A. Schell, and D. Deering, "Monitoring vegetation systems in the great plains with ERTS," in *Proc. 3rd Symp. Significant Results Obtained 1st Earth Resour. Technol. Satell.*, pp. 301–317 1973.
- [58] L. Breiman, "Bagging predictors," *Mach. Learn.*, vol. 24, no. 2, pp. 123–140, Aug. 1996.
- [59] S. V. Stehman, "Selecting and interpreting measures of thematic classification accuracy," *Remote Sens. Environ.*, vol. 62, no. 1, pp. 301–317, Oct. 1997.
- [60] D. Powers, "Evaluation: From precision, recall and F-factor to ROC, informedness, markedness and correlation," *Mach. Learn. Technol.*, vol. 2, Jan. 2008.
- [61] J. R. Landis and G. G. Koch, "The measurement of observer agreement for categorical data," *Biometrics*, vol. 33, no. 1, pp. 159–74, 1977.
- [62] C. Sammut and G. I. Webb, Eds., *Leave-One-Out Cross-Validation*. Boston, MA, USA: Springer, 2010, pp. 301–317.
- [63] Z. Jiang, A. R. Huete, K. Didan, and T. Miura, "Development of a two-band enhanced vegetation index without a blue band," *Remote Sens. Environ.*, vol. 112, no. 10, pp. 3833–3845, 2008.
- [64] E. Hunt and B. N. Rock, "Detection of changes in leaf water content using near- and middle-infrared reflectances," *Remote Sens. Environ.*, vol. 30, no. 1, pp. 43–54, 1989.
- [65] "Detection of forest harvest type using multiple dates of landsat TM imagery," *Remote Sens. Environ.*, vol. 80, no. 3, pp. 385–396, 2002.
- [66] T. Fawcett, "An introduction to ROC analysis," *Pattern Recognit. Lett.*, vol. 27, no. 8, pp. 861–874, 2006.



Vahid Akbari (Member, IEEE) received the M.Sc. degree in remote sensing (*summa cum laude*) from the University of Tehran, Tehran, Iran, in 2009 and the Ph.D. degree in physics majoring in earth observation from the UiT The Arctic University of Norway, Tromsø, Norway, in 2013.

He continued his research in radar remote sensing as a Postdoctoral Research Fellow with the Department of Physics and Technology, UiT The Arctic University of Norway. He was a Visiting Scientist with the Signal Processing and Telecommunications

Laboratory, Department of Electrical, Electronic, Telecommunications Engineering and Naval Architecture, University of Genoa, Genoa, Italy, in 2011, and a Visiting Researcher with German Geoscience Center (GFZ), Potsdam, Germany, in 2008. He was an Assistant Professor of Remote Sensing with the University of Tehran in 2015. He has been an Adviser for seven M.Sc. students and two Ph.D. students. He is currently a Research Scientist in earth observation with Division of Forest and Forest Resources of the Norwegian Institute of Bioeconomy Research. His research interests include development of methods to extract information on land and ocean with radar remote sensing data. His focus is mainly on the use of interferometric and polarimetric SAR from satellite, and aircraft sensors for studies of land deformation, land cover classification, and change detection, marine target detection and characterization in polar regions, as well as monitoring forest disturbance and resources.



Svein Solberg received the M.Sc. degree in forestry in 1985 and the Dr. Agric. degree in forest health monitoring in 1999. University of life sciences, Ås, Norway.

Since 1990, he has been a Researcher with the Norwegian Forest and Landscape Institute (now the Norwegian Institute of Bioeconomy Research) Ås, Norway. During 2008–2013, he had a professorship in environmental monitoring with the Norwegian University of Life Sciences (NMBU), Ås, Norway. He has worked on a variety of remote sensing technologies

and has developed methods for deriving leaf area index and single-tree segmentation from airborne laser scanning. In recent years, he has focused on SAR and, in particular, interferometric X-band SAR and radargrammetry for monitoring of volume and biomass, as well as detection of logging and storm damage. He has authored or coauthored 43 papers published in international peer-reviewed journals. His major field of research is on monitoring forest disturbance and resources, partly based on remote sensing methods.



Stefano Puliti received a double M.Sc. degree in European forestry with particular focus on forest remote sensing from the Swedish University of Agricultural Science (SLU), Umeå, Sweden and the University of Eastern Finland (UEF), Joensuu, Finland, in 2012 and the Ph.D. degree in forest inventory and remote sensing from the Norwegian University of Life Sciences (NMBU), Ås, Norway, in 2017.

Since 2017, he has been a Research Scientist with the Department of National Forest Inventory, the Division of Forestry and Forest Resources, Norwegian Institute for Bioeconomy Research (NIBIO), Ås, Norway. During the past decade, he conducted research on the use of 3-D remotely sensed data (e.g., Lidar, photogrammetry) as well as satellite data for forest resource assessment. During the Ph.D. and currently much of his work has been devoted to the use of drones as platforms to collect advanced data analytics for precision forestry purposes. Complementarily to developing small-scale applications using drones, he developed skills in satellite image processing for mapping and estimating biomass and biomass changes.